Optical Parametric Generation in a Lithium Niobate Microring with Modal Phase Matching

Rui Luo,[1,†] Yang He,[2,†] Hanxiao Liang,[2] Mingxiao Li,[2] Jingwei Ling,[1] and Qiang Lin[1,2,*]

[1]*Institute of Optics, University of Rochester, Rochester, New York 14627, USA*

[2]*Department of Electrical and Computer Engineering, University of Rochester, Rochester, New York 14627, USA*

The lithium niobate integrated photonic platform has recently shown great promise in nonlinear optics on a chip scale. Here, we report second-harmonic generation in a high-Q lithium niobate microring resonator through modal phase matching, with a conversion efficiency of 1500% W^{-1}. Our device also allows us to observe difference-frequency generation in the telecom band. Our work demonstrates the great potential of the lithium niobate integrated platform for nonlinear wavelength conversion with high efficiencies.

I. INTRODUCTION

Optical parametric generation via a quadratic nonlinearity has been extensively studied for the capability of wavelength conversion through elastic photon-photon scattering, constituting the basis of various applications, including coherent radiation [1], spectroscopy [2], frequency metrology [3], and quantum-information processing [4]. With the ability to strongly confine optical modes at the micro/nanoscale, a number of integrated photonic platforms have been developed for strong nonlinear optical effects with high efficiencies and low power consumption [5–11].

Among all the integrated nonlinear photonic platforms, lithium niobate (LN) has recently attracted remarkable attention, owing to its wide transparency window and strong quadratic optical nonlinearity. To date, a variety of nanophotonic systems, including waveguides [12–18], microdisks [19–24], microrings [25,26], and photonic crystal cavities [27–29], have been studied for optical parametric processes in LN. In particular, cavity-enhanced nonlinear wavelength conversion has been demonstrated in doubly or triply resonant LN microresonators through a number of techniques, including modal phase matching [19,22,24,26], cyclic phase matching [20,21,23], and quasi-phase-matching [25]. However, the potential of the LN integrated platform has not yet been fully explored for efficient nonlinear parametric processes and current devices demonstrate only moderate efficiencies far from what LN can provide. Here, we report optical parametric generation in a high-Q Z-cut LN microring resonator through exact modal phase matching. The device exhibits

optical Q's of around 10^5 for the designed cavity modes in the 1550- and 780-nm bands, and both modes are well coupled to a single bus waveguide, enabling us to conveniently measure a second-harmonic generation (SHG) efficiency of 1500% W^{-1}. In addition, by pumping into the mode in the 780-nm band, we are also able to observe difference-frequency generation (DFG) in the telecom band. Our work shows the great promise of modal-phase-matched LN microresonators for efficient optical parametric generation.

II. DESIGN AND CHARACTERIZATION

In order to achieve modal phase matching in a microresonator, we perform photonic design with a Z-cut LN thin film, whose optic axis lies vertically, showing no anisotropy of its refractive index in the device plane. To utilize the largest nonlinear term d_{33}, we design for phase matching between the fundamental quasi-transverse-magnetic mode (TM_{00}) at 1550 nm and a high-order mode TM_{20} at 775 nm. For simplicity, we numerically simulate effective indices of optical modes in a straight waveguide, as a guideline for microring resonators with a relatively large radius, which is 50 μm in our study. Figure 1(b) presents the simulation result by the finite-element method, which shows that, for a waveguide thickness of 600 nm, modal phase matching happens for TM_{00} at 1550 nm and TM_{20} at 775 nm when the waveguide width is about 690 nm. For a microring resonator with the same cross section, since the Z-cut LN thin film is isotropic in the device plane, the phase-matching condition is consistently satisfied at any azimuthal angle, which is expected to produce strong SHG as the phase-matched fundamental-frequency (FF) light travels around the cavity.

Our device fabrication starts from a Z-cut LN-on-insulator wafer by NANOLN, with a 600-nm-thick LN

---
*qiang.lin@rochester.edu

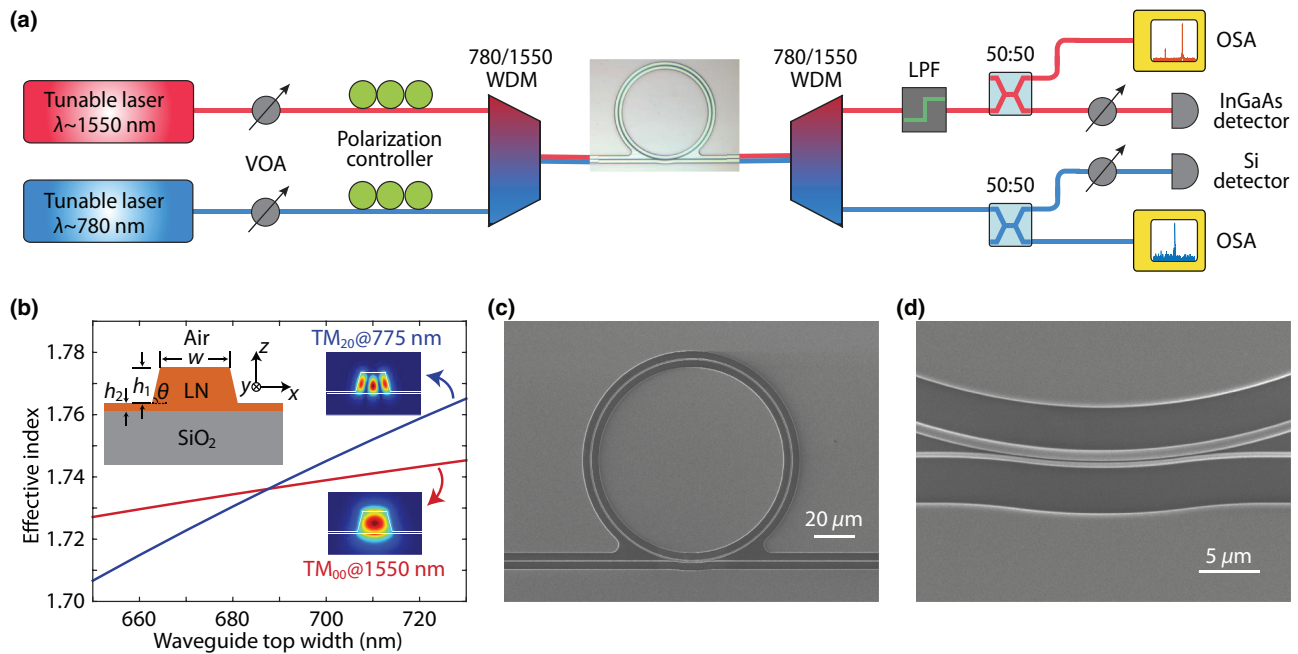†These two authors contributed equally.

FIG. 1.   (a) Experimental setup for device characterization and optical parametric generation. VOA denotes variable optical attenuator; WDM, wavelength-division multiplexer; LPF, long-pass filter; and OSA, optical spectrum analyzer. (b) Numerically simulated effective indices of the TM_{00} mode at 1550 nm and the TM_{20} mode at 775 nm, as functions of the top width w of a straight waveguide. Other waveguide parameters are $h_1 = 550$ nm, $h_2 = 50$ nm, and $\theta = 75°$. (c) Scanning electron microscopy image of our LN microring. (d) Enlargement of the bus-ring coupling region.

thin film sitting on a 3-μm-thick buried oxide layer and a silicon substrate, and the process is similar to that of our previous work [29]. Figure 1(c) shows a fabricated microring resonator, coupled to a pulley waveguide [30,31], and Fig. 1(d) gives a closer look at the coupling region. Later device characterization shows that a bus waveguide top width of approximately 200 nm, a gap (measured at the top surface of the LN thin film) of approximately 350 nm, and a coupling length of approximately 20 μm are able to give good coupling for both the FF mode and the second-harmonic (SH) mode.

After fabricating the device, we conduct experiments to characterize its linear optical properties and demonstrate nonlinear parametric generation, with the setup shown in Fig. 1(a). We use two continuous-wave tunable lasers, one in the telecom band around 1550 nm, the other in the near-infrared (NIR) around 780 nm. Light from both lasers is combined by a 780/1550 wavelength-division multiplexer (WDM), and launched into the on-chip bus waveguide via a lensed fiber. The bus waveguide couples light at both wavebands into and out of the microring resonator, inside of which nonlinear optical parametric processes take place. A second lensed fiber is used to collect output light from the chip and a second 780/1550 WDM is utilized to separate light at the two wavebands. At the 1550 port of the WDM, a long-pass filter that passes light with a wavelength over 1100 nm is used to eliminate residual NIR light

and the telecom light is further split into two paths, one to an InGaAs detector for characterization, and the other to an optical spectrum analyzer (OSA) for spectral analysis of DFG; at the 780 port, the NIR light is also split into two paths, one to a Si detector for characterization, and the other to an OSA for detection of SHG. Variable optical attenuators are employed to study power-dependent properties and polarization controllers are used for optimal coupling of the wanted polarization.

In order to obtain the linear optical properties of our microring resonator, we scan the wavelengths of both lasers and measure the transmission spectra near both 1550 and 780 nm, as shown in Figs. 2(a) and 2(b). Our microring resonator exhibits a single TM mode family near 1550 nm, and the mode at 1547.10 nm, which is the FF mode for modal-phase-matched SHG, is almost critically coupled, with a coupling depth of approximately 99% and a loaded optical Q of 1.4×10^5 [see Fig. 2(c)]. On the other hand, the SH mode at 773.55 nm is undercoupled, with a coupling depth of approximately 83% and a loaded optical Q of 9×10^4 [see Fig. 2(d)]. To achieve phase matching, the FF and SH resonances are fine-tuned by controlling the temperature with a thermoelectric cooler under the device chip. The fiber-to-chip coupling losses are about 6.9 and 11.4 dB/facet for the FF and SH modes, respectively. These high optical Q's, together with the large nonlinearity in the designed type-0 process using
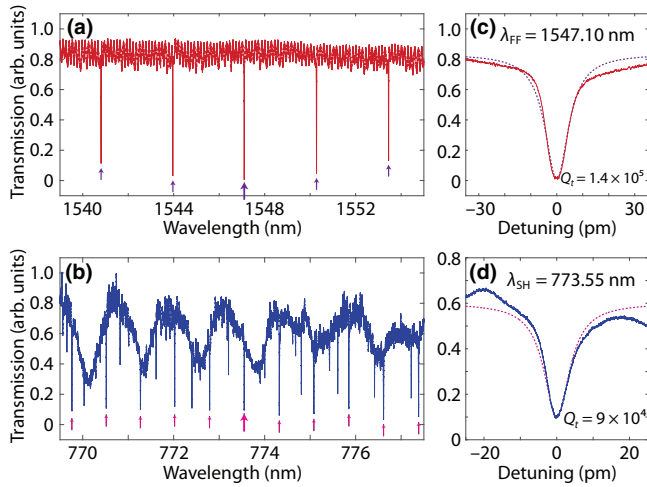
FIG. 2. Transmission spectra of the LN microring near (a) 1550 nm and (b) 780 nm. TM_{00} modes around 1550 nm and TM_{20} modes around 780 nm are indicated by purple and magenta arrows, respectively, with big arrows showing the phase-matched modes. (c),(d) Detailed transmission spectra of the two phase-matched modes, with experimental data shown in solid curves and fittings shown in dashed curves.

d_{33}, indicate strong and efficient nonlinear optical interactions in phase-matched parametric generation with cavity enhancement.

III. OPTICAL PARAMETRIC GENERATION

To study SHG in the microring resonator, we launch pump power into the FF mode at 1547.10 nm and observe strong scattering of generated NIR light from the resonator by an optical microscope, with an example shown in the inset of Fig. 3. By varying the pump power, we obtain the power dependence of the SHG, as shown in Fig. 3. The experimental data exhibit a quadratic relation between the generated SH power and the FF pump power, which is the signature of SHG in the low-pump-power regime. The measured conversion efficiency is 1500% W^{-1}. This efficiency is more than 1 order of magnitude higher than those in many other LN microresonators [19–21,24–29]. It is even comparable with a recent study of cyclic phase matching in an X-cut microdisk exhibiting an ultrahigh Q of approximately 10^7 [23], 2 orders of magnitude higher than that of our microring resonator, due to the use of modal phase matching that offers a major advantage. With future optimization of the optical Q's of our device (e.g., by using a thicker LN film and an oxide cladding to reduce the sidewall scattering loss), we expect a further increase in the conversion efficiency.

The measured efficient SHG validates phase matching in our microring and also indicates its capability for other parametric processes. In order to explore this, we launch power in both the SH mode and one of the modes near
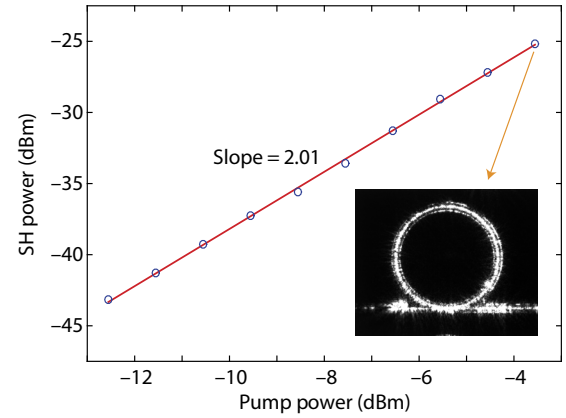

FIG. 3. Power dependence of SHG, showing a quadratic relation between the SH power and the pump power. The measured conversion efficiency is 1500% W^{-1}. The inset shows an optical image of generated NIR light scattered from the microring, with a pump power of 440 μW at the FF mode.

the FF mode. Figure 4 presents the recorded spectra in the telecom band. With only 6.6 μW of on-chip power at the SH mode, we are able to convert long-wavelength telecom light coherently into shorter wavelengths through DFG. The long-wavelength pump power launched on the chip is 105 μW and the generated power at the difference frequencies is about 480 pW, indicating a conversion rate of about -53 dB.

IV. THEORETICAL ANALYSIS

In order to acquire a better understanding of nonlinear parametric processes in our device, we analyze the system with a model derived from the coupled-mode theory [32,33]. The conversion efficiency is calculated with numerically simulated modes of the waveguide and experimentally measured Q-factors of the microring resonator
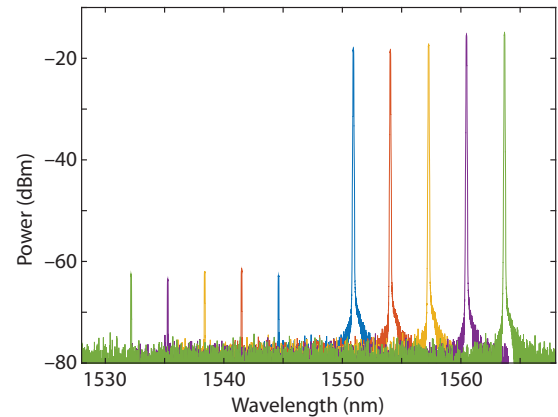

FIG. 4. Recorded DFG spectra, when pumping at the SH mode in the NIR and one of the five nearest modes with longer wavelengths than the FF mode in the telecom band. Pump power at the SH mode is 6.6 μW.

(see Appendix A for details). Using this model, the SHG efficiency in our LN microring is calculated to be $\Gamma \approx 30\,000\%\ \mathrm{W}^{-1}$. Thus, there is a difference of more than 1 order of magnitude between the theoretical prediction and the experimental result.

The main reason for this discrepancy is likely nonuniformity of the microring at different azimuthal angles. By simulation, a change of 1 nm in the waveguide width, for example, leads to a shift of approximately -3 nm in the phase-matched pump wavelength of SHG. Considering the small linewidths of our cavity modes, which are only 11 pm for the FF mode and 9 pm for the SH mode, the local phase-matching window at some azimuthal angle is easily shifted out of the cavity resonances due to fabrication imperfections (see Appendix B for details). In the current work, relevant fabrication imperfections include the noncircular beam spot in electron-beam lithography, the proximity effect in lithography and etching, and the nonuniformity in the thickness of the LN thin film, all of which could prevent the fabricated microring from exhibiting perfect rotational symmetry. We believe this efficiency degradation can be resolved by optimized fabrication techniques in the near future and the conversion efficiency can be significantly improved.

V. CONCLUSION

In conclusion, we demonstrate optical parametric generation in a LN microring resonator with modal phase matching. We use a single bus waveguide to conveniently couple the FF and SH modes, both exhibiting coupling depths of over 80% and loaded optical Q's of around 10^5, resulting in a measured conversion efficiency of $1500\%\ \mathrm{W}^{-1}$ for SHG. In addition, we also observe DFG in the telecom band. Our work represents an important step toward ultrahighly efficient optical parametric generation in photonic circuits based on the LN integrated platform.

ACKNOWLEDGMENTS

APPENDIX A: DERIVATION OF SHG EFFICIENCY IN AN OPTICAL RESONATOR

The analytical model of the cavity-enhanced nonlinear optical parametric processes is derived from the coupled-mode theory [32,33]. For simplicity, the material anisotropy is not fully accounted for. The derivation is first performed to obtain the coupling strength between two cavity modes assuming no optical losses, and loss terms and laser-cavity detunings are added in the simplified equations later.

SHG induced by the quadratic nonlinear interaction is described by driven wave equations as

$$\nabla^2 \tilde{\mathbf{E}}_1(\mathbf{r}, t) - \frac{\epsilon(\mathbf{r}, \omega_1)}{c^2} \frac{\partial^2}{\partial t^2} \tilde{\mathbf{E}}_1(\mathbf{r}, t) = \frac{1}{\epsilon_0 c^2} \frac{\partial^2}{\partial t^2} \tilde{\mathbf{P}}_1^{NL}(\mathbf{r}, t),$$
(A1)

$$\nabla^2 \tilde{\mathbf{E}}_2(\mathbf{r}, t) - \frac{\epsilon(\mathbf{r}, \omega_2)}{c^2} \frac{\partial^2}{\partial t^2} \tilde{\mathbf{E}}_2(\mathbf{r}, t) = \frac{1}{\epsilon_0 c^2} \frac{\partial^2}{\partial t^2} \tilde{\mathbf{P}}_2^{NL}(\mathbf{r}, t),$$
(A2)

where c and ϵ_0 are the speed of light and permittivity in vacuum, respectively; $\epsilon(\mathbf{r}, \omega_1)$ [$\epsilon(\mathbf{r}, \omega_2)$] is the relative permittivity; ω_1 (ω_2) is the angular optical frequency at the FF (SH), with $\omega_2 = 2\omega_1$; and the nonlinear polarizations are represented as

$$\tilde{\mathbf{P}}_1^{NL}(\mathbf{r}, t) = \epsilon_0 \chi^{(2)}(\omega_1; -\omega_1, \omega_2) \tilde{\mathbf{E}}_1^*(\mathbf{r}, t) \tilde{\mathbf{E}}_2(\mathbf{r}, t), \quad \text{(A3)}$$

$$\tilde{\mathbf{P}}_2^{NL}(\mathbf{r}, t) = \frac{\epsilon_0}{2} \chi^{(2)}(\omega_2; \omega_1, \omega_1) \tilde{\mathbf{E}}_1(\mathbf{r}, t) \tilde{\mathbf{E}}_1(\mathbf{r}, t). \quad \text{(A4)}$$

In an optical resonator, when ω_1 and ω_2 are near the frequencies of two cavity resonances, the electric fields can be written as

$$\tilde{\mathbf{E}}_1(\mathbf{r}, t) = A_1(t) \mathbf{E}_1(\mathbf{r}) e^{-i\omega_{10} t}, \quad \text{(A5)}$$

$$\tilde{\mathbf{E}}_2(\mathbf{r}, t) = A_2(t) \mathbf{E}_2(\mathbf{r}) e^{-i\omega_{20} t}, \quad \text{(A6)}$$

where ω_{10} and ω_{20} are the resonance frequencies that are close to phase matching, i.e., $\Delta\omega \equiv \omega_{20} - 2\omega_{10} \ll \min(\omega_{\mathrm{FSR},1}, \omega_{\mathrm{FSR},2})$, with $\omega_{\mathrm{FSR},1}$ and $\omega_{\mathrm{FSR},2}$ being the free-spectral ranges; $\mathbf{E}_1(\mathbf{r})$ and $\mathbf{E}_2(\mathbf{r})$ are the mode profiles in the three-dimensional cavity; and $A_1(t)$ and $A_2(t)$ are the field amplitudes. By substituting Eqs. (A3)–(A6) into Eqs. (A1)–(A2), the relation between the coupled field

amplitudes is obtained as

$$\frac{dA_1}{dt}\epsilon(\mathbf{r},\omega_{10})\mathbf{E}_1(\mathbf{r}) = \frac{i\omega_{10}}{2}A_1^*A_2e^{-i\Delta\omega t}\chi^{(2)}\mathbf{E}_1^*(\mathbf{r})\mathbf{E}_2(\mathbf{r}),$$
(A7)

$$\frac{dA_2}{dt}\epsilon(\mathbf{r},\omega_{20})\mathbf{E}_2(\mathbf{r}) = \frac{i\omega_{20}}{4}A_1^2e^{i\Delta\omega t}\chi^{(2)}\mathbf{E}_1(\mathbf{r})\mathbf{E}_1(\mathbf{r}),$$
(A8)

where slowly evolving amplitudes, $|d^2A_j/dt^2| \ll |\omega_{j0}(dA_j/dt)|$, and weak dispersion, $\epsilon(\mathbf{r},\omega_j) \approx \epsilon(\mathbf{r},\omega_{j0})$ ($j = 1, 2$), have been assumed. Also, it has been considered that the mode profiles, $\mathbf{E}_1(\mathbf{r})$ and $\mathbf{E}_2(\mathbf{r})$, satisfy

$$\nabla^2\mathbf{E}_1(\mathbf{r}) + \epsilon(\mathbf{r},\omega_{10})\frac{\omega_{10}^2}{c^2}\mathbf{E}_1(\mathbf{r}) = 0,$$
(A9)

$$\nabla^2\mathbf{E}_2(\mathbf{r}) + \epsilon(\mathbf{r},\omega_{20})\frac{\omega_{20}^2}{c^2}\mathbf{E}_2(\mathbf{r}) = 0.$$
(A10)

By multiplying $\mathbf{E}_1^*(\mathbf{r})$ on both sides of Eq. (A7), multiplying $\mathbf{E}_2^*(\mathbf{r})$ on both sides of Eq. (A8), and integrating both equations over all three-dimensional space, Eqs. (A7)–(A8) become

$$\frac{dA_1}{dt} = \frac{i\omega_{10}}{2}A_1^*A_2e^{-i\Delta\omega t}\frac{\int \chi_{ijk}^{(2)}E_{1i}^*E_{1j}^*E_{2k}d^3x}{\int \epsilon(\mathbf{r},\omega_{10})|\mathbf{E}_1|^2d^3x},$$
(A11)

$$\frac{dA_2}{dt} = \frac{i\omega_{20}}{4}A_1^2e^{i\Delta\omega t}\frac{\int \chi_{ijk}^{(2)}E_{2i}^*E_{1j}E_{1k}d^3x}{\int \epsilon(\mathbf{r},\omega_{20})|\mathbf{E}_2|^2d^3x},$$
(A12)

where Einstein summation convention has been used. The amplitudes can be normalized as

$$a_1'(t) = A_1(t)\sqrt{\frac{\epsilon_0}{2}\int \epsilon(\mathbf{r},\omega_{10})|\mathbf{E}_1(\mathbf{r})|^2d^3x},$$
(A13)

$$a_2'(t) = A_2(t)\sqrt{\frac{\epsilon_0}{2}\int \epsilon(\mathbf{r},\omega_{20})|\mathbf{E}_2(\mathbf{r})|^2d^3x},$$
(A14)

such that $|a_1'|^2$ and $|a_2'|^2$ represent intracavity optical energies.

The amplitudes can be further normalized as

$$a_1(t) = \frac{a_1'(t)}{\sqrt{\hbar\omega_{10}}},$$
(A15)

$$a_2(t) = \frac{a_2'(t)}{\sqrt{\hbar\omega_{20}}},$$
(A16)

such that $|a_1|^2$ and $|a_2|^2$ represent intracavity photon numbers, with

$$\frac{da_1}{dt} = \frac{i\omega_{10}}{2}\sqrt{\frac{2\hbar\omega_{20}}{\epsilon_0}}a_1^*a_2e^{-i\Delta\omega t}$$
$$\times \frac{\int \chi_{ijk}^{(2)}E_{1i}^*E_{1j}^*E_{2k}d^3x}{\int \epsilon(\mathbf{r},\omega_{10})|\mathbf{E}_1|^2d^3x\sqrt{\int \epsilon(\mathbf{r},\omega_{20})|\mathbf{E}_2|^2d^3x}},$$
(A17)

$$\frac{da_2}{dt} = \frac{i\omega_{10}}{4}\sqrt{\frac{2\hbar\omega_{20}}{\epsilon_0}}a_1^2e^{i\Delta\omega t}$$
$$\times \frac{\int \chi_{ijk}^{(2)}E_{2i}^*E_{1j}E_{1k}d^3x}{\int \epsilon(\mathbf{r},\omega_{10})|\mathbf{E}_1|^2d^3x\sqrt{\int \epsilon(\mathbf{r},\omega_{20})|\mathbf{E}_2|^2d^3x}}.$$
(A18)

Equations (A17)–(A18) can be simplified when only one nonlinear medium is in the system. In this case, the mode overlap factor is written as

$$\zeta_{ijk} = \frac{\int_{\chi^{(2)}} E_{2i}^*E_{1j}E_{1k}d^3x}{|\int_{\chi^{(2)}}|\mathbf{E}_1|^2\mathbf{E}_1d^3x|^{2/3}|\int_{\chi^{(2)}}|\mathbf{E}_2|^2\mathbf{E}_2d^3x|^{1/3}},$$
(A19)

where $\int_{\chi^{(2)}}$ and $\int_{\text{all}}$ denote integration over the nonlinear medium and all space, respectively, and the effective mode volume can be defined as $V_{\text{eff}} \equiv (V_1^2V_2)^{1/3}$, with

$$V_j = \frac{[\int_{\text{all}}\epsilon(\mathbf{r},\omega_{j0})|\mathbf{E}_j|^2d^3x]^3}{|\int_{\chi^{(2)}}\epsilon(\mathbf{r},\omega_{j0})^{3/2}|\mathbf{E}_j|^2\mathbf{E}_jd^3x|^2}, \quad (j = 1, 2).$$
(A20)

As a result, the single-photon coupling strength is written as

$$\gamma = \sqrt{\frac{\hbar\omega_{10}^2\omega_{20}}{8\epsilon_0\tilde{\epsilon}_1^2\tilde{\epsilon}_2}}\frac{\chi_{ijk}^{(2)}\zeta_{ijk}}{\sqrt{V_{\text{eff}}}},$$
(A21)

where $\tilde{\epsilon}_1$ and $\tilde{\epsilon}_2$ are the relative permittivity of the nonlinear medium at ω_{10} and ω_{20}, respectively. Equation (A21) is a general form of the coupling strength for SHG in an optical cavity.

In the current work, the mode overlap factor has a dominant contribution from $\int_{\chi^{(2)}} E_{2z}^*E_{1z}^2d^3x$ due to $\chi_{333}^{(2)}$; thus, it can be simplified to

$$\zeta = \frac{\int_{\chi^{(2)}} E_{2z}^*E_{1z}^2d^3x}{|\int_{\chi^{(2)}}|\mathbf{E}_1|^2\mathbf{E}_1d^3x|^{2/3}|\int_{\chi^{(2)}}|\mathbf{E}_2|^2\mathbf{E}_2d^3x|^{1/3}}.$$
(A22)

For a rotationally symmetric microring with a relatively large radius, the transverse mode profiles can be approximated by those of the corresponding waveguide modes,

$\mathbf{E}_1^{(\mathrm{wg})}$ and $\mathbf{E}_2^{(\mathrm{wg})}$; thus, the overlap factor can be further represented as that of the waveguide, i.e.,

$$\zeta = \zeta^{(\mathrm{wg})}$$
$$= \frac{\int_{\chi^{(2)}} (E_{2z}^{(\mathrm{wg})})^* (E_{1z}^{(\mathrm{wg})})^2 dxdz}{|\int_{\chi^{(2)}} |\mathbf{E}_1^{(\mathrm{wg})}|^2 \mathbf{E}_1^{(\mathrm{wg})} dxdz|^{2/3} |\int_{\chi^{(2)}} |\mathbf{E}_2^{(\mathrm{wg})}|^2 \mathbf{E}_2^{(\mathrm{wg})} dxdz|^{1/3}}. \tag{A23}$$

Similarly, the effective volume of the cavity can be represented as the product of the waveguide effective area $A_{\mathrm{eff}}^{(\mathrm{wg})}$ and the cavity length L, i.e., $V_{\mathrm{eff}} = A_{\mathrm{eff}}^{(\mathrm{wg})} L$, where $A_{\mathrm{eff}}^{(\mathrm{wg})} \equiv [(A_1^{(\mathrm{wg})})^2 A_2^{(\mathrm{wg})}]^{1/3}$, with

$$A_j^{(\mathrm{wg})} = \frac{[\int_{\mathrm{all}} \epsilon(\mathbf{r}, \omega_{j0}) |\mathbf{E}_j^{(\mathrm{wg})}|^2 dxdz]^3}{|\int_{\chi^{(2)}} \epsilon(\mathbf{r}, \omega_{j0})^{3/2} |\mathbf{E}_j^{(\mathrm{wg})}|^2 \mathbf{E}_j^{(\mathrm{wg})} dxdz|^2}, (j = 1, 2). \tag{A24}$$

Therefore, the coupling strength can then be written as

$$\gamma = \sqrt{\frac{\hbar \omega_{10}^2 \omega_{20}}{2\epsilon_0 \tilde{\epsilon}_1^2 \tilde{\epsilon}_2}} \frac{d_{\mathrm{eff}} \zeta^{(\mathrm{wg})}}{\sqrt{A_{\mathrm{eff}}^{(\mathrm{wg})} L}}, \tag{A25}$$

where $d_{\mathrm{eff}} = d_{33} = \chi_{333}^{(2)}/2$. Note that Eq. (A25) only contains basic physical quantities of the cavity, and information about the optical modes is from the corresponding waveguide. As a result, the coupled-mode equations can be simplified to

$$\frac{da_1}{dt} = 2i\gamma^* e^{-i\Delta\omega t} a_1^* a_2, \tag{A26}$$

$$\frac{da_2}{dt} = i\gamma e^{i\Delta\omega t} a_1^2. \tag{A27}$$

When the two cavity modes have finite linewidths and external pump fields, the driven coupled-mode equations can be written as

$$\frac{da_1}{dt} = -\frac{\kappa_{1t}}{2} a_1 + 2i\gamma^* e^{-i\Delta\omega t} a_1^* a_2 + i\sqrt{\kappa_{1e}} F_1 e^{-i\delta_1 t}, \tag{A28}$$

$$\frac{da_2}{dt} = -\frac{\kappa_{2t}}{2} a_2 + i\gamma e^{i\Delta\omega t} a_1^2 + i\sqrt{\kappa_{2e}} F_2 e^{-i\delta_2 t}, \tag{A29}$$

where κ_{1t} (κ_{2t}) is the total cavity loss rate, κ_{1e} (κ_{2e}) is the external coupling rate, and $\delta_1 \equiv \omega_1 - \omega_{10}$ ($\delta_2 \equiv \omega_2 - \omega_{20}$) is the laser-cavity detuning of the FF (SH), and F_1 (F_2) is the amplitude of the driving field at ω_1 (ω_2). In a SHG

process, only the FF mode is externally pumped, leading to

$$\frac{da_1}{dt} = -\frac{\kappa_{1t}}{2} a_1 + 2i\gamma^* e^{-i\Delta\omega t} a_1^* a_2 + i\sqrt{\kappa_{1e}} F_1 e^{-i\delta_1 t}, \tag{A30}$$

$$\frac{da_2}{dt} = -\frac{\kappa_{2t}}{2} a_2 + i\gamma e^{i\Delta\omega t} a_1^2. \tag{A31}$$

In order to remove the slowly oscillating factors, $e^{\pm i\Delta\omega t}$ and $e^{-i\delta_1 t}$, Eqs. (A30)–(A31) can be written in a rotating reference frame ($a_1 \to a_1 e^{-i\delta_1 t}$, $a_2 \to a_2 e^{-i\delta_2 t}$), which yields

$$\frac{da_1}{dt} = (i\delta_1 - \frac{\kappa_{1t}}{2}) a_1 + 2i\gamma^* a_1^* a_2 + i\sqrt{\kappa_{1e}} F_1, \tag{A32}$$

$$\frac{da_2}{dt} = [i(2\delta_1 - \Delta\omega) - \frac{\kappa_{2t}}{2}] a_2 + i\gamma a_1^2, \tag{A33}$$

where the energy conservation law, $\omega_2 = \omega_{20} + \delta_2 = 2(\omega_{10} + \delta_1) = 2\omega_1$, has been applied to obtain $\delta_2 = 2\delta_1 - \Delta\omega$. In this case, an amplitude can be defined as $G_2 = i\sqrt{\kappa_{2e}} a_2$, with $|G_2|^2$ representing the flux of SH photons at the cavity output.

In the weak-conversion regime without pump depletion, i.e., $|a_1| \gg |a_2|$, the cross term in Eq. (A32) is negligible and Eq. (A32) can be simplified to

$$\frac{da_1}{dt} = (i\delta_1 - \frac{\kappa_{1t}}{2}) a_1 + i\sqrt{\kappa_{1e}} F_1. \tag{A34}$$

For a continuous-wave pump, the steady state requires $da_1/dt = da_2/dt = 0$ in Eqs. (A33)–(A34) and the normalized amplitudes are written as

$$a_1 = \frac{i\sqrt{\kappa_{1e}} F_1}{(\kappa_{1t}/2) - i\delta_1}, \tag{A35}$$

$$a_2 = \frac{i\gamma a_1^2}{(\kappa_{2t}/2) - i(2\delta_1 - \Delta\omega)}. \tag{A36}$$

Thus, the relation between the pump photon flux, $N_1 = |F_1|^2$, and the output SH photon flux, $N_2 = |G_2|^2$, is obtained as

$$N_2 = N_1^2 |\gamma|^2 \frac{\kappa_{1e}^2}{[(\kappa_{1t}/2)^2 + \delta_1^2]^2} \frac{\kappa_{2e}}{(\kappa_{2t}/2)^2 + (2\delta_1 - \Delta\omega)^2}. \tag{A37}$$

With the input FF power, $P_1 = N_1 \hbar \omega_1$, and the output SH power, $P_2 = N_2 \hbar \omega_2$, the conversion efficiency can be calculated as

$$\Gamma \equiv \frac{P_2}{P_1^2} = \frac{|\gamma|^2 \omega_2}{\hbar \omega_1^2} \frac{\kappa_{1e}^2}{[(\kappa_{1t}/2)^2 + \delta_1^2]^2} \frac{\kappa_{2e}}{(\kappa_{2t}/2)^2 + (2\delta_1 - \Delta\omega)^2}. \tag{A38}$$

In the case of exact phase matching and on-resonance pumping, i.e., $\Delta\omega = \delta_1 = 0$, Eq. (A38) can be written with

regard to quality factors, $Q_{t(e)} = \omega/\kappa_{t(e)}$, as follows:

$$\Gamma = \frac{64|\gamma|^2}{\hbar\omega_1^4} \frac{Q_{1t}^4 Q_{2t}^2}{Q_{1e}^2 Q_{2e}}. \quad \text{(A39)}$$

Equation (A39) is used to calculate the maximal conversion efficiency in the current device.

APPENDIX B: EFFICIENCY DEGRADATION DUE TO INCONSISTENT LOCAL PHASE MATCHING

For the two cavity modes involved in SHG, the resonance frequencies are determined by the overall resonant condition of the resonator (related to the total phase shift per round trip), given as

$$\frac{\omega_{10}}{c}\bar{n}_1(\omega_{10})L \equiv \frac{\omega_{10}}{c}\int_0^{2\pi} n_1(\omega_{10},\phi)Rd\phi = 2m_1\pi, \quad \text{(B1)}$$

$$\frac{\omega_{20}}{c}\bar{n}_2(\omega_{20})L \equiv \frac{\omega_{20}}{c}\int_0^{2\pi} n_2(\omega_{20},\phi)Rd\phi = 2m_2\pi, \quad \text{(B2)}$$

where R is the cavity radius; $\bar{n}_1$ and $\bar{n}_2$ are the effective refractive indices averaged over the cavity; and m_1 and m_2 are the azimuthal mode orders, with $m_2 = 2m_1$. Even with fabrication imperfections, global phase matching can be conveniently achieved between the two cavity modes, i.e., $\omega_{20} = 2\omega_{10}$ and $\bar{n}_2(\omega_{20}) = \bar{n}_1(\omega_{10})$.

Despite the global phase matching, the measured SHG efficiency can be lower than the theoretical prediction, due to imperfect rotation symmetry of the fabricated device. As shown in Eq. (A22), the SHG efficiency is determined by the mode overlap between the two cavity modes over the whole cavity,

$$\zeta \propto \int_{\chi^{(2)}} E_{2z}^* E_{1z}^2 d^3x = \xi \int_{\chi^{(2)}} (E_{2z}^{(T)})^* (E_{1z}^{(T)})^2 d\rho dz, \quad \text{(B3)}$$

where ρ is the radial coordinate in cylindrical coordinates; $\mathbf{E}_1^{(T)}(\rho,z)$ and $\mathbf{E}_2^{(T)}(\rho,z)$ are the transverse mode profiles of the cavity modes; and ξ is an integrated phase mismatch factor, written as

$$\xi = \frac{1}{L}\int_0^{2\pi} e^{i\frac{\omega_{20}}{c}[n_2(\omega_{20},\phi)-n_1(\omega_{10},\phi)]R\phi} Rd\phi. \quad \text{(B4)}$$

In the ideal case with $n_1(\omega_{10},\phi) = n_2(\omega_{20},\phi) = \text{const}$ at any azimuthal angle, ξ has a maximal value of 1, leading to the maximal conversion efficiency calculated by Eq. (A39). However, the ϕ-dependent variations of $n_1(\omega_{10},\phi)$ and $n_2(\omega_{20},\phi)$, which are introduced by fabrication imperfections, can decrease the value of ξ, resulting in a degraded conversion efficiency.

[1] Malcolm H. Dunn and Majid Ebrahimzadeh, Parametric generation of tunable light from continuous-wave to femtosecond pulses, Science **286,** 1513 (1999).

[2] K. Fradkin, A. Arie, A. Skliar, and G. Rosenman, Tunable midinfrared source by difference frequency generation in bulk periodically poled KTiOPO$_4$, Appl. Phys. Lett. **74,** 914 (1999).

[3] Steven T. Cundiff and Jun Ye, Colloquium: Femtosecond optical frequency combs, Rev. Mod. Phys. **75,** 325 (2003).

[4] Jian-Wei Pan, Zeng-Bing Chen, Chao-Yang Lu, Harald Weinfurter, Anton Zeilinger, and Marek Żukowski, Multiphoton entanglement and interferometry, Rev. Mod. Phys. **84,** 777 (2012).

[5] Luigi Scaccabarozzi, M. M. Fejer, Yijie Huo, Shanhui Fan, Xiaojun Yu, and James S. Harris, Enhanced second-harmonic generation in AlGaAs/Al$_x$O$_y$ tightly confining waveguides and resonant cavities, Opt. Lett. **31,** 3626 (2006).

[6] Kelley Rivoire, Ziliang Lin, Fariba Hatami, W. Ted Masselink, and Jelena Vučković, Second harmonic generation in gallium phosphide photonic crystal nanocavities with ultralow continuous wave pump power, Opt. Express **17,** 22609 (2009).

[7] Jacob S. Levy, Mark A. Foster, Alexander L. Gaeta, and Michal Lipson, Harmonic generation in silicon nitride ring resonators, Opt. Express **19,** 11415 (2011).

[8] M. Cazzanelli, F. Bianco, E. Borga, G. Pucker, M. Ghulinyan, Elena Degoli, E. Luppi, V. Véniard, Stefano Ossicini, D. Modotto, S. Wabnitz, R. Pierobon, and L. Pavesi, Second-harmonic generation in silicon waveguides strained by silicon nitride, Nat. Mat. **11,** 148 (2012).

[9] Paulina S. Kuo, Jorge Bravo-Abad, and Glenn S. Solomon, Second-harmonic generation using-quasi-phasematching in a GaAs whispering-gallery-mode microcavity, Nat. Commun. **5,** 3109 (2014).

[10] Xiang Guo, Chang-Ling Zou, and Hong X. Tang, Second-harmonic generation in aluminum nitride microrings with 2500%/W conversion efficiency, Optica **3,** 1126 (2016).

[11] E. Timurdogan, Christopher V. Poulton, M. J. Byrd, and M. R. Watts, Electric field-induced second-order nonlinear optical effects in silicon waveguides, Nat. Photon. **11,** 200 (2017).

[12] Reinhard Geiss, Sina Saravi, Anton Sergeyev, Séverine Diziain, Frank Schrempel, Rachel Grange, Ernst-Bernhard Kley, Andreas Tünnermann, and Thomas Pertsch, Fabrication of nanoscale lithium niobate waveguides for second-harmonic generation, Opt. Lett. **40,** 2715 (2015).

[13] Lin Chang, Yifei Li, Nicolas Volet, Leiran Wang, Jon Peters, and John E. Bowers, Thin film wavelength converters for photonic integrated circuits, Optica **3,** 531 (2016).

[14] Cheng Wang, Xiao Xiong, Nicolas Andrade, Vivek Venkataraman, Xi-Feng Ren, Guang-Can Guo, and Marko Loncar, Second harmonic generation in nano-structured thin-film lithium niobate waveguides, Opt. Express **25,** 6963 (2017).

[15] Ashutosh Rao, Jeff Chiles, Saeed Khan, Seyfollah Toroghi, Marcin Malinowski, Guillermo Fernando Camacho González, and Sasan Fathpour, Second-harmonic

generation in single-mode integrated waveguides based on mode-shape modulation, Appl. Phys. Lett. **110,** 111109 (2017).

[16] Rui Luo, Yang He, Hanxiao Liang, Mingxiao Li, and Qiang Lin, Highly tunable efficient second-harmonic generation in a lithium niobate nanophotonic waveguide, Optica **5,** 1006 (2018).

[17] Lutong Cai, Andrey V. Gorbach, Yiwen Wang, Hui Hu, and Wei Ding, Highly efficient broadband second harmonic generation mediated by mode hybridization and nonlinearity patterning in compact fiber-integrated lithium niobate nano-waveguides, Sci. Rep. **8,** 12478 (2018).

[18] Rui Luo, Yang He, Hanxiao Liang, Mingxiao Li, and Qiang Lin, Semi-nonlinear nanophotonic waveguides for highly efficient second-harmonic generation, Laser Photon. Rev. **13,** 1800288 (2019).

[19] Cheng Wang, Michael J. Burek, Zin Lin, Haig A. Atikian, Vivek Venkataraman, I.-Chun Huang, Peter Stark, and Marko Loncar, Integrated high quality factor lithium niobate microdisk resonators, Opt. Express **22,** 30924 (2014).

[20] Jintian Lin, Yingxin Xu, Jielei Ni, Min Wang, Zhiwei Fang, Lingling Qiao, Wei Fang, and Ya Cheng, Phase-matched Second-harmonic Generation in an On-chip LiNbO$_3$ Microresonator, Phys. Rev. Appl. **6,** 014002 (2016).

[21] Rui Luo, Haowei Jiang, Steven Rogers, Hanxiao Liang, Yang He, and Qiang Lin, On-chip second-harmonic generation and broadband parametric down-conversion in a lithium niobate microresonator, Opt. Express **25,** 24531 (2017).

[22] Zhenzhong Hao, Jie Wang, Shuqiong Ma, Wenbo Mao, Fang Bo, Feng Gao, Guoquan Zhang, and Jingjun Xu, Sum-frequency generation in on-chip lithium niobate microdisk resonators, Photon. Res. **5,** 623 (2017).

[23] Jintian Lin, Yao Ni, Zhenzhong Hao, Jianhao Zhang, Wenbo Mao, Min Wang, Wei Chu, Rongbo Wu, Zhiwei Fang, Lingling Qiao, Wei Fang, Fang Bo, and Ya Cheng, Highly-efficient second and third harmonic generation in a monocrystalline lithium niobate microresonator, arXiv:1809.04523 (2018).

[24] Li Wang, Cheng Wang, Jie Wang, Fang Bo, Mian Zhang, Qihuang Gong, Marko Loncar, and Yun-Feng Xiao, High-Q chaotic lithium niobate microdisk cavity, Opt. Lett. **43,** 2917 (2018).

[25] Richard Wolf, Yuechen Jia, Sebastian Bonaus, Christoph S. Werner, Simon J. Herr, Ingo Breunig, Karsten Buse, and Hans Zappe, Quasi-phase-matched nonlinear optical frequency conversion in on-chip whispering galleries, Optica **5,** 872 (2018).

[26] Jia-Yang Chen, Yong Meng Sua, Heng Fan, and Yu-Ping Huang, Modal phase matched lithium niobate nanocircuits for integrated nonlinear photonics, OSA Continuum **1,** 229 (2018).

[27] Séverine Diziain, Reinhard Geiss, Matthias Zilk, Frank Schrempel, Ernst-Bernhard Kley, Andreas Tünnermann, and Thomas Pertsch, Second harmonic generation in freestanding lithium niobate photonic crystal L3 cavity, Appl. Phys. Lett. **103,** 051117 (2013).

[28] Haowei Jiang, Hanxiao Liang, Rui Luo, Xianfeng Chen, Yuping Chen, and Qiang Lin, Nonlinear frequency conversion in one dimensional lithium niobate photonic crystal nanocavities, Appl. Phys. Lett. **113,** 021104 (2018).

[29] Mingxiao Li, Hanxiao Liang, Rui Luo, Yang He, and Qiang Lin, High-Q two-dimensional lithium niobate photonic crystal slab nanoresonators, arXiv:1806.04755 (2018).

[30] Ehsan Shah Hosseini, Siva Yegnanarayanan, Amir Hossein Atabaki, Mohammad Soltani, and Ali Adibi, Systematic design and fabrication of high-Q single-mode pulley-coupled planar silicon nitride microdisk resonators at visible wavelengths, Opt. Express **18,** 2127 (2010).

[31] Xiyuan Lu, Qing Li, Daron A. Westly, Gregory Moille, Anshuman Singh, Vikas Anant, and Kartik Srinivasan, Chip-integrated visible-telecom photon pair sources for quantum communication, arXiv:1805.04011 (2018).

[32] Robert W Boyd, *Nonlinear Optics* (Academic, New York, 2008), 3rd ed.

[33] Alejandro Rodriguez, Marin Soljačić, John D. Joannopoulos, and Steven G. Johnson, $\chi^{(2)}$ and $\chi^{(3)}$ harmonic generation at a critical power in inhomogeneous doubly resonant cavities, Opt. Express **15,** 7303 (2007).